AIAA 81-0191R

Implicit Solution for the Shock-Layer Flow around General Bodies

C. P. Li*
NASA Lyndon B. Johnson Space Center, Houston, Texas

The simplified forms of the Navier-Stokes equations are solved by an iterative implicit scheme along the body axis for angles of incidence up to 30 deg. The method of solution yields both the inviscid and viscous flows simultaneously and predicts bow shock at stations normal to the axis. The technique is developed from a comparatively simple linearization procedure and has an option to iterate between body stations for higher accuracy. Reliable procedures have been introduced to account for the effect of the axial pressure gradient and to adjust the step increment for a given convergence requirement. A blunt cone and a Shuttle Orbiter-like configuration were studied and good agreement is obtained with available laminar boundary-layer solutions and experimental data.

Introduction

VISCOUS flowfield solutions around a re-entry vehicle are needed for the prediction of heating distributions as well as for the interpretation of aerodynamic data to support the design and flight test processes. The traditional boundary-layer (BL) approach that decouples the viscous flow from the outer inviscid flow has been valuable in the past; however, for the problems of current interest, such as the Space Shuttle Orbiter and the maneuverable re-entry vehicle, a more accurate solution is being obtained from the coupled fluid dynamics equations. This paper presents a method suitable for complex configurations that may be described by a lofting technique used by the aerospace industry. The method is devised to solve the Euler equations for the inviscid region and the parabolic Navier-Stokes (PNS) equations for the viscous region along an identifiable main-flow direction. The PNS equations are obtained from the full NS equation by omitting the second-order and the mixed derivatives and by approximating the exact pressure gradient in the designated direction. The flowfield of interest is bounded between the shock, the body, an initial-data plane normal to the specified direction, and a downstream station parallel to the initial plane. Although the length scales associated with the flow phenomena differ greatly on that plane, highly nonuniform grid spacings near the wall are not desirable in practice, as the shock must be calculated accurately. Hence, a detailed shock-layer solution requires a large number of grid points and consequently long computation time. In return for its cost, this method does not have any of the known shortcomings associated with the BL analyses and offers new capabilities for predicting leeside flow and crossflow separation. For this reason, there has been an intensive research effort in this decade to solve for the viscous flow as an integral part of the flowfield.

Many studies of the three-dimensional steady supersonic flow past simple configurations have been reported in the literature. The potential of the methodology was first demonstrated by Lubard and Helliwell[1] in the analysis of the crossflow separation on a sharp cone. In later years, collaborations with other authors have resulted in the studies of the flowfield around a blunt cone[2] and around a biconic body with an asymmetric slice and cut.[3] The formulation was originally based on body-normal coordinates, then developed for both body- and shock-normal coordinates. The numerical scheme is similar to an earlier version reported by Lin and Rubin[4] for analyzing the leading-edge flow on a cone. It has an iterative feature ensuring that the complete equation be solved implicitly, even though a portion of the equation is partly explicit. A different method for calculating aerodynamic flow at arbitrary speeds has been developed in recent years. The method uses a generalized coordinate transformation that relates the flow vectors defined in Cartesian coordinates to those in body-conforming coordinates. The resulting strongly conservative-form equations are solved by a noniterative factorization technique that replaces the solution of a multidimensional implicit equation with that of a sequence of one-dimensional implicit equations. Applications of this method include the sharp and blunt cone flowfields by Schiff and Steger[5] and the delta-wing study by Vigneron et al.[6] One of the simplest body shapes studied was the supersonic flow over a flat plate by Nardo and Cresci[7] using an alternating directional implicit (ADI) technique and by Li[8] using a splitting implicit technique. The two techniques seem to be more suited for flows undergoing rapid axial changes such as near the leading and side edges of a flat configuration.

Some of the problems have been studied with the method developed by Murray and Lewis.[9] Their equations are derived from the NS equation by achieving parabolicity in both the streamwise and circumferential directions of the flow. The standard iterative technique for solving the BL equations is applied to the decoupled equations until all variables converge to a prescribed tolerance. The crossflow separated region is calculated subsequently by the method of Ref. 1, using the attached flow variables as boundary conditions on the crossflow plane. If the surrounding shock shape is given a priori from an inviscid analysis, this method has been shown to yield a solution equivalent to the PNS solution but at significantly less computation time.

These achievements have motivated the author to develop a method applicable to blunt-nosed noncircular bodies with longitudinal curvature such as the Space Shuttle Orbiter. The flowfield calculation around the vehicle is more difficult than that for earlier cases because of rapid pressure variations in the streamwise direction at the nose and near the swept wing as well as by the strong crossflow expansion at high angles of attack around the bottom corner. Also, it is desirable to develop a more flexible method to predict the bow shock for regions where the shock intersects the body. The flowfield between the fuselage and the swept wing is so complicated

Presented as Paper 81-0191 at the AIAA 19th Aerospace Sciences Meeting, St. Louis, Mo., Jan. 12-14, 1981; submitted Feb. 20, 1981; revision received June 26, 1981. This paper is declared a work of the U.S. Government and therefore is in the public domain.

*Research Engineer, Aerothermodynamics Section. Member AIAA.

that the problem is presently circumvented by approximating the realistic cross section with a delta shape. The formulation of governing equations is based on the cylindrical coordinate system, which allows the marching solution to be executed easily along the body axis and minimizes the number of metrics. The computational procedure described in Ref. 8 is modified to accommodate the factorization technique developed by Beam and Warming[10] or, from a different viewpoint, the noniterative factorization technique described in Ref. 10 is modified to include iterations. The iterations may be helpful to maintain the consistency and accuracy of the solution, since the nonlinearity of flow fluxes and the mixed derivatives on the crossflow plane can be important and should be accounted for fully. The number of iterations needed to satisfy a given tolerance is related to the marching step increment; hence, it is hoped that with iterations performed between two stations, the method will provide optimal efficient solutions. The shock location is determined by the slope at the previous station, whereas the new shock slope is obtained from a fitting procedure after the flow variables are converged at the new station. The reader is referred to a parallel but independent effort carried out by Chaussee et al.[11] for calculating viscous flows around a similar vehicle.

Numerical Method

Equations in Computation Space

The governing equations are formulated on cylindrical coordinates aligned with the body axis. The computational coordinates, created by means of simple analytical transformations, correspond to nonuniform grid lines between the shock and the body and in between the pitch planes. The basic formulation, excluding the viscous terms, resembles the inviscid work by Kutler et al.[12] in their studies of supersonic flow over an Orbiter vehicle. As mentioned in the Introduction, in order to use the marching technique, the full NS equations are made parabolic along the body axis by eliminating the mixed and the second-order derivatives involving the axial coordinate. Thus, the Euler or PNS equations and the continuity and energy equations formulated for the shock-layer flow become a set of partial differential equations having first-order derivatives in the marching axis.

Letting the computational coordinates be denoted by (x,y,z), the governing equations may be expressed symbolically by the following equation:

$$f_x+g_y+h_z+r=0 \tag{1}$$

where

$$x=\xi$$

$$y=\sinh[\beta(s-\eta)/(s-b)]/\sinh\beta$$

$$z=\pi[c+\sinh^{-1}[(\zeta/\zeta_0-1)\sinh(\omega c)]/\omega]$$

$$c=\ell n\{[1+(e^{\omega}-1)\zeta_0/\pi]/[1+(e^{-\omega}-1)\zeta_0/\pi]\}/2\omega$$

The physical coordinates are (ξ,η,ζ); the parameters β, ω, and ζ_0 are used to control the nonuniformity of the coordinates near the body and at the angular location ζ_0, respectively. The vectors f, g, h, and r are related to those defined on cylindrical coordinates by means of metrics

$$f=f \qquad g=y_\xi\bar{f}+y_\eta\bar{g}+y_\zeta\bar{h} \qquad h=z_\zeta\bar{h} \qquad r=\bar{r}$$

The metrics y_ξ, etc., are nondifferentiable variable relating the computational to the physical coordinates. The vectors have the following form:

$$f=\begin{bmatrix}\rho u\\ \rho u^2+p\\ \rho uv\\ \rho uw\\ \rho u\epsilon\end{bmatrix} \quad \bar{f}=\begin{bmatrix}\rho u\\ \rho u^2+\pi_{\xi\xi}\\ \rho uv+\pi_{\xi\eta}\\ \rho uw+\pi_{\xi\zeta}\\ \rho u\epsilon+\phi_\xi\end{bmatrix} \quad \bar{g}=\begin{bmatrix}\rho v\\ \rho vu+\pi_{\eta\xi}\\ \rho v^2+\pi_{\eta\eta}\\ \rho vw+\pi_{\eta\zeta}\\ \rho v\epsilon+\phi_\eta\end{bmatrix}$$

$$\bar{h}=\frac{1}{\eta}\begin{bmatrix}\rho w\\ \rho wu+\pi_{\zeta\xi}\\ \rho wv+\pi_{\zeta\eta}\\ \rho w^2+\pi_{\zeta\zeta}\\ \rho w\epsilon+\phi_\zeta\end{bmatrix} \quad \bar{r}=\frac{1}{\eta}\begin{bmatrix}\rho v\\ \rho vu\\ \rho(v^2-w^2)\\ 2\rho vw\\ \rho v\epsilon+pv\end{bmatrix}$$

where ρ is the density; u, v, and w the velocity components in ξ, η, and ζ; and ϵ the total internal energy. The pressure and internal energy are obtained from $p=(\gamma-1)\rho e$, and $e=\epsilon-0.5(u^2+v^2+w^2)$ for a perfect gas, whereas the temperature $T=e/c_v$, c_v is the specific heat at constant volume.

Finite-Difference Equations

An application of the differencing schemes described by Richtmyer and Morton[13] for solving the heat equation led to the difference equation that corresponds to Eq. (1).

$$(1+\sigma)(f^{N+1}_{\ell,M}-f^{N}_{\ell,M})-\sigma(f^{N}_{\ell,M}-f^{N-1}_{\ell,M})$$
$$+\frac{\Delta x}{2\Delta y}[\tau(g^{N+1}_{\ell,M+1}-g^{N+1}_{\ell,M-1})+(1-\tau)(g^{N}_{\ell,M+1}-g^{N}_{\ell,M-1})]$$
$$+\frac{\Delta x}{2\Delta z}[\tau(h^{N+1}_{\ell+1,M}-h^{N+1}_{\ell-1,M})+(1-\tau)(h^{N}_{\ell+1,M}-h^{N}_{\ell-1,M})]$$
$$+\Delta x r^{N}_{\ell,M}=0 \tag{2}$$

Among five possible variations, only two are of practical interest in the solution for the Euler and PNS equations: the Laasonen scheme ($\sigma=0$, $\tau=1$) and the Richtmyer scheme ($\sigma=0.5$, $\tau=1$). The truncation errors in Δx are of first and second order, whereas the errors in Δy and Δz are of second order. Since the accuracy of the flow variables is determined by the magnitude of Δx, the similarity of the flowfield, etc., the best approach to ensure consistency in the solutions other than resorting to a small Δx is probably by means of iterations between stations N and $N+1$. The iterative version of Eq. (2) is shown as follows for $\tau=1$:

$$\delta f^{K+1}_{\ell,M}+\frac{1}{1+\sigma}\frac{\Delta x}{2\Delta y}(\delta g^{K+1}_{\ell,M+1}-\delta g^{K+1}_{\ell,M-1})+\frac{1}{1+\sigma}\frac{\Delta x}{2\Delta z}$$
$$\times(\delta h^{K+1}_{\ell+1,M}-\delta h^{K+1}_{\ell-1,M})=\phi^{K}_{\ell,M} \tag{3}$$

where

$$\delta f^{K+1}_{\ell,M}=f^{K+1}_{\ell,M}-f^{K}_{\ell,M}, \text{ etc.}$$

$$\phi^{K}_{\ell,M}=\frac{\sigma}{1+\sigma}\delta f^{N}_{\ell,M}-f^{K}_{\ell,M}+f^{N}_{\ell,M}-\frac{1}{1+\sigma}\frac{\Delta x}{2\Delta y}(g^{K}_{\ell,M+1}-g^{K}_{\ell,M-1})$$
$$-\frac{1}{1+\sigma}\frac{\Delta x}{2\Delta z}(h^{K}_{\ell+1,M}-h^{K}_{\ell-1,M})-\frac{\Delta x}{1+\sigma}r^{N}_{\ell,M}$$

Using K to denote the iterative sequence, the iteration starts with $K=1$, $f^{K}_{\ell,M}=f^{N}_{\ell,M}$, etc., and terminates at $K=K$, $f^{N+1}_{\ell,M}=$

$f^K_{\ell,M}$ when $|\delta f^K_{\ell,M}/f^K_{\ell,M}| \le c$ for all points. The tolerance c is a prescribed value. The viscous fluxes in f, g, and h are obtained from either one-sided or centered formulas using the average viscosity and heat conductivity between two points.

A solvable form can be arranged for Eq. (3) using the approximate linearization procedure described in Ref. 8, which in essence defines the relationships between δf, δg, δh, and δv. The primitive variables constitute the vector v in $v^T = (\rho,u,v,w,e)$. The explicit forms of linearization are

$$\delta f_{\ell,M} = A_{\ell,M}\delta v_{\ell,M}$$

$$\delta g_{\ell,M\pm1} = B_{\ell,M\pm1}\delta v_{\ell,M\pm1} \mp 2E_{\ell,M\pm1}(\delta v_{\ell,M\pm1} - \delta v_{\ell,M})/\Delta y$$

$$\delta h_{\ell\pm1,M} = C_{\ell\pm1,M}\delta v_{\ell\pm1,M} \mp 2F_{\ell\pm1,M}(\delta v_{\ell\pm1,M} - \delta v_{\ell,M})/\Delta z$$

The superscript may be either K, $K+1$, or N. These relations are not necessarily rigorous because the differencing counterparts of the cross derivatives are excluded. Therefore, the iterative difference equation will become more reliable to govern the flow variables when the neglected mixed difference quotients are important.

Iterative Factored Algorithm

Two operators are introduced to perform the following functions:

$$D_y\delta v_{\ell,M} = \delta g_{\ell,M+1} - \delta g_{\ell,M-1}$$

$$D_z\delta v_{\ell,M} = \delta h_{\ell+1,M} - \delta h_{\ell-1,M}$$

Thus, Eq. (3) can be recast in the linearized form

$$A_{\ell,M}\delta v_{\ell,M} + \frac{1}{1+\sigma}\frac{\Delta x}{2\Delta y}D_y\delta v_{\ell,M} + \frac{1}{1+\sigma}\frac{\Delta x}{2\Delta z}D_z\delta v_{\ell,M} = \phi^K_{\ell,M} \quad (4)$$

Equation (4) may be solved by the factored algorithm and the resultant equations are given in Eq. (5).

$$\left(A_{\ell,M} + \frac{1}{1+\sigma}\frac{\Delta x}{2\Delta y}D_y\right)\delta v^*_{\ell,M} = \phi^K_{\ell,M}$$

$$\left(A_{\ell,M} + \frac{1}{1+\sigma}\frac{\Delta x}{2\Delta z}D_z\right)\delta v^{K+1}_{\ell,M} = A_{\ell,M}\delta v^*_{\ell,M} \quad (5)$$

The factored technique has been used for solving unsteady fluid dynamics equations by Beam and Warming[10] and Pulliam and Steger[14] for unknown variables $u^T = (\rho,\rho u,\rho v,\rho w,\rho\epsilon)$. Briley and McDonald[15] used an ADI version ($\tau=0.5$, $\sigma=0$) to seek for unknown variables $v^T = (\rho,u,v,w,T)$. The present procedure is developed by first linearizing the difference equation and then factoring the component equations. It is in contrast to the procedure presented in Ref. 8, which splits the equation before linearizing each component equation. Both procedures solve for $v^T = (\rho,u,v,w,e)$ and permit a simple derivation of Jacobian matrices; namely, A, B, C, E, and F (see the Appendix).

The two equations shown in Eq. (5) are each of a system of tridiagonal equations for grid points within the computation domain

$$a_{\ell,M}\delta v^*_{\ell,M-1} + b_{\ell,M}\delta v^*_{\ell,M} + c_{\ell,M}\delta v^*_{\ell,M+1} = \phi^K_{\ell,M} \quad (6a)$$

$$d_{\ell,M}\delta v^{K+1}_{\ell-1,M} + e_{\ell,M}\delta v^{K+1}_{\ell,M} + f_{\ell,M}\delta v^{K+1}_{\ell+1,M} = A^K_{\ell,M}\delta v^*_{\ell,M} \quad (6b)$$

The coefficients are

$$a_{\ell,M} = \frac{-1}{1+\sigma}\frac{\Delta x}{2\Delta y}\left(B_{\ell,M-1} + \frac{2}{\Delta y}E_{\ell,M-1}\right)$$

$$b_{\ell,M} = A_{\ell,M} + \frac{2}{1+\sigma}\frac{\Delta x}{(\Delta y)^2}E_{\ell,M}$$

$$c_{\ell,M} = \frac{1}{1+\sigma}\frac{\Delta x}{2\Delta y}\left(B_{\ell,M+1} - \frac{2}{\Delta y}E_{\ell,M+1}\right)$$

$$d_{\ell,M} = \frac{-1}{1+\sigma}\frac{\Delta x}{2\Delta z}\left(C_{\ell-1,M} + \frac{2}{\Delta z}F_{\ell-1,M}\right)$$

$$e_{\ell,M} = A_{\ell,M} + \frac{2}{1+\sigma}\frac{\Delta x}{(\Delta z)^2}F_{\ell,M}$$

$$f_{\ell,M} = \frac{1}{1+\sigma}\frac{\Delta x}{2\Delta z}\left(C_{\ell+1,M} - \frac{2}{\Delta z}F_{\ell+1,M}\right)$$

for $\ell=3$ through $\ell=LCM$ and $M=3$ through $M=MCM$.

Boundary Conditions

Four boundary lines, depicted in Fig. 1 for both physical and computational planes, are to be considered. The flow is symmetric to the pitch plane, $z=0$ and π. Hence, $v_z(y,0) = v_z(y,\pi) = 0$ for ρ, u, v, e, p, and T and $v(y,0) = v(y,\pi) = 0$ for w. The source term on the right side of Eq. (6b) is calculated from $v_{M,1} = v_{M,3}$ for ρ, u, v, e, p, and T and $v_{M,1} = -v_{M,3}$ for w, and the coefficients $d_{2,M}$ and $f_{LC,M}$ are combined with $e_{2,M}$ and $e_{LC,M}$, respectively, in order to close the tridiagonal system of equations. The additional equations appended to Eq. (6b) are as follows:

$$\bar e_{2,M}\delta v^{K+1}_{2,M} + f_{2,M}\delta v^{K+1}_{3,M} = A_{2,M}\delta v^*_{2,M}$$

$$d_{LC,M}\delta v^{K+1}_{LCM,M} + \bar e_{LC,M}\delta v^{K+1}_{LC,M} = A_{LC,M}\delta v^*_{LC,M} \quad (7a)$$

where

$$\bar e_{2,M} = e_{2,M} + d_{2,M}, \quad \bar e_{LC,M} = e_{LC,M} + f_{LC,M} \text{ for } \rho,u,v,\text{etc.}$$

$$\bar e_{2,M} = e_{2,M} - d_{2,M}, \quad \bar e_{LC,M} = e_{LC,M} - f_{LC,M} \text{ for } w$$

The third and fourth boundaries purposely are made to coincide with the shock and the wall at $y=0$ and $y=1$, respectively. The shock location is estimated from $s^{N+1}_\ell = s^N_\ell + (s_x)^N_\ell \Delta x$. The source term in Eq. (6a) is calculated at this line using one-side difference and the coefficient $a_{\ell,1}$ is equal to zero. A new $(s_x)^{N+1}_\ell$ is obtained from the fitting procedure matching the Rankine-Hugoniot velocity normal to the shock with the same component predicted at $N+1$ from the Euler equation. The decoupling of shock shape from the flowfield solution is a simple and successful means established in the earlier inviscid calculations.[12] The no-slip velocity and cooled-wall conditions can be easily and accurately implemented into Eq. (6a). The only variable to be calculated on the wall is $\rho_{\ell,MC}$ which can be obtained from the relations $p_{\ell,MCM} = p_{\ell,MC}$ and $\delta e_{\ell,MC} = 0$ for $(e_y)_w \neq 0$ or $\delta e_{\ell,MC} = \delta e_{\ell,MCM}$

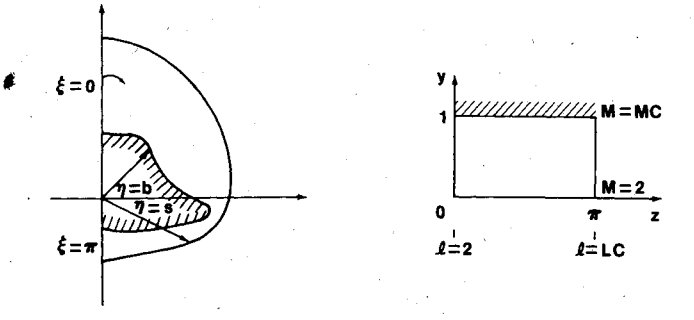

Fig. 1 Cross-sectional view of the flowfield on the physical and computational planes.

for $(e_y)_w = 0$. Hence,

$$\delta\rho_{\ell,MC} = (T_{\ell,MCM}\delta\rho_{\ell,MCM} + \rho_{\ell,MCM}\delta T_{\ell,MCM})/T_{\ell,MC}$$

and

$$\delta u_{\ell,MC} = \delta v_{\ell,MCM} = \delta w_{\ell,MC} = 0$$

The additional equations supplemental to Eq. (6a) are summarized as follows:

$$\bar{b}_{\ell,2}\delta v^*_{\ell,2} + c_{\ell,2}\delta v^*_{\ell,3} = \phi^K_{\ell,2}$$

$$a_{\ell,MCM}\delta v^*_{\ell,MCM-1} + \bar{b}_{\ell,MCM}\delta v^*_{\ell,MCM} = \phi^K_{\ell,MCM} \qquad (7b)$$

where

$$\bar{b}_{\ell,2} = b_{\ell,2}$$

$$\bar{b}_{\ell,MCM} = b_{\ell,MCM} \quad \text{for } u, v, w$$

$$= b_{\ell,MCM} + c_{\ell,MCM}T_{\ell,MCM}/T_{\ell,MC} \quad \text{for } \rho$$

$$= b_{\ell,MCM} + c_{\ell,MCM}\rho_{\ell,MCM}/(c_v T_{\ell,MC}) \quad \text{for } T_{\ell,MCM} \neq T_{\ell,MC}$$

With all points defined heretofore, a block-tridiagonal procedure described in Ref. 8 is applied to solve Eqs. (6) and (7).

Axis-Normal Solution

Figure 2 is a sketch of three axial stations on the leeside pitch plane in the physical and computational coordinate systems. The body and shock slopes are constant between two stations. The solution at the $N+1$ station uses the local b and s and the local geometry metrics. The first guess of the solution is that already known at station N. The step size should be a constant value so that the Richtmyer scheme can be used. In practice, the magnitude of Δx is based on the anticipated changes between stations. They can vary from $0.05R$ in regions of rapid changes to $0.5R$ in regions exhibiting strong similarity (where R is the nose radius of the vehicle). If Δx is too large, it can be halved automatically. The decision is made by comparing the max $|\delta\rho/\rho|_{\ell,M}$ at $K=1$ with a prescribed tolerance c ranging from 0.05 to 0.005. If max $|\delta\rho/\rho|_{\ell,M} > c$ even after Δx is halved, the solution to Eq. (6) will be iterated more than once.

Another parameter y^* is introduced to approximately delineate the inviscid and viscous regions within the shock layer. In essence, the Euler equations are solved for $0 \le y < y^*$ and the PNS equations are solved for $y^* \le y \le 1$. However, a simultaneous solution is still obtained for grid points across the shock layer and in between the pitch planes. With the aid of y^*, a damping term of third-order magnitude is incorporated for inviscid flow calculations.

Axial Pressure Gradient

The stability analyses of Refs. 5 and 8 have shown clearly that the p variable in f must be treated differently from other variables for $y^* \le y \le 1$. Nearly all procedures for solving the PNS equations have adopted one means or another to account for the effect of the axial pressure gradient. The most plausible one is probably the approach using the lagged pressure gradient.[1-8] However, a straightforward application of lagged p_x has little success in a region where the flow experiences overexpansion and recompression because of the amplification of error in the pressure field along the axis. The fluctuation of pressures on the axis-normal plane is another source for errors in the downstream calculation. A more stable gradient of pressure may be obtained from the following procedure. A nondimensional gradient $(d\ell np/dx)_\ell$ is estimated at N station using the average pressure values between $y^* \le y \le 1$ for each ℓ plane. When p_x is needed at (ℓ, M), it is obtained from $(p_x)^{N+1}_{\ell,M} = p^N_{\ell,M}(d\ell np/dx)^N_\ell$. The overall accuracy does not seem to be affected by the magnitude of y^*, whose value may range from 0.7 to 0.95. However, y^* must be sufficiently large to ensure $M^*_x > 1$ for stability considerations.

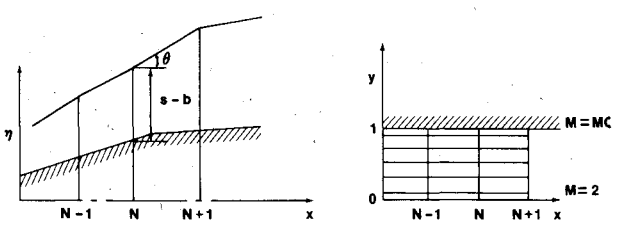

Fig. 2 Axial stations on the physical and computational coordinates.

Initial Data

The initial data station is usually downstream of the blunt nose and located beyond the sonic surface; its actual location varies with the freestream conditions and the nose shape. In order to have the initial data ρ, u, v, w, e, p_x, b, and s defined, one must solve the transonic flow at the nose region. The method of solution is similar to the present one but it has distinguishing features that need lengthy description. A separate report is planned to give a full account of the nose solutions. If the initial data are consistent and accurate, the marching procedure will proceed smoothly along the axis; otherwise, the error tends to stay with the viscous solution and the marching procedure frequently fails to predict reasonable heat flux and shear stress at all.

Body Geometry

The cross section and the longitudinal slope of the vehicle are obtained from the lofting technique described by Meyers.[16] Using the blueprint as a guide, the cross section can be represented by seven or less analytical segments and they are connected by spline-fitted curves following the longitudinal variations. This technique results in a set of body coefficients that can be used at an arbitrary axial station and angular orientation to define the body and its slopes. Figure 3

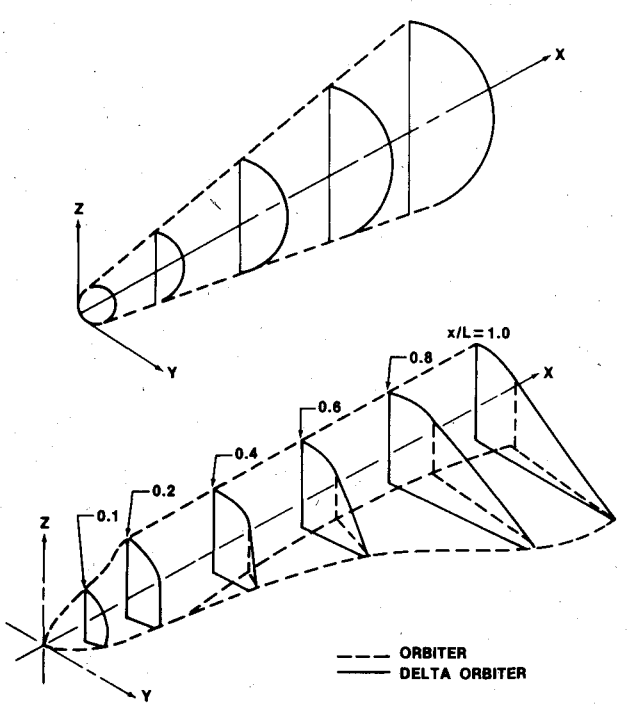

Fig. 3 Body configurations used for shock-layer computations; a) spherical cone, b) Shuttle Orbiter.

illustrates a perspective view of body configuration considered in the study. The Orbiter representation is realistic from the nose to the station at $x/L=0.25$ with the exception of the canopy. Beyond $x/L=0.25$, the delta configuration only resembles the Orbiter on both the windward and leeside surfaces. The cross section is made of four segments: a top ellipse, a straight line, a cubic arc, and a bottom ellipse.

Discussion of Results

Since the PNS solutions have been shown to be in good agreement with experimental data of wall pressures, shock locations, crossflow separation, etc.,[1-8] it is the purpose of this section to bring out the comparison with the viscous-related parameters. In particular, the shear stress and the heating rates obtained from the boundary-layer theory[17] and the wind-tunnel test[18,19] are compared with their counterparts from the PNS solution. The transverse profiles of static and total temperatures are likewise compared and discussed. Two sets of freestream conditions, both corresponding to the AEDC Tunnel B environment, are used in the study. The first two cases are a spherical cone at $M_\infty=8$, $Re_\infty=0.213\times10^6$/m, $p_\infty=0.0995$ kg/m^2, and $\alpha=0$ and 15 deg, where α is the angle of attack. The third case is a delta-shaped Orbiter at $M_\infty=8$, $Re_\infty=0.335\times10^6$/m, $p_\infty=0.138$ kg/m^2, and $\alpha=30$ deg. All these cases have been calculated with a variety of grid systems; however, only the results obtained from the grid with sufficient spatial resolutions are presented.

Case 1 is devoted to the parametric studies on the basis of an axisymmetric flow over a spherical cone of 15 deg half-angle. The effects of the step size, iterations, initial data, and the pressure gradient along the axis are analyzed individually and the results are used to guide the calculation of two other nontrivial cases. The main difference between the PNS and the BL solution is demonstrated by analyzing the transverse profiles of temperature across the shock layer. Figure 4a shows the temperature profiles from the BL theory superimposed on the profiles from the inviscid calculation. The edge conditions having variable entropy are more representative of the realistic viscous flow than the conditions having normal shock entropy. However, even the entropy-swallowing boundary layer is significantly different from the coupled inviscid-viscous flowfield in the displacement effects and values of frictional temperature. The prominent higher temperature predicted by the PNS solution in Fig. 4b suggests that more work has been done by the coupled viscous layer than by the decoupled boundary layer. The slightly different directions along which the temperature profiles are given do not cause the difference in temperature. A plot of the total temperature profile across the shock layer (not shown) locates the edge of the viscous layer at 10-15% of the shock layer.

The second case, a spherical cone at $\alpha=15$ deg, has been studied in considerable depth. The calculations are made using one iteration ($K=2$) with the initial data plane at $x/R=1$. The step increments are prescribed as a function of the axial distance measured from the nose tip. They vary from $0.1R$ at $x/R=1$ to $0.25R$ at $x/R=30$. A large Δx can be used near the end of the calculation because the flowfield evolves into the conical pattern as x increases. Figure 5a shows the wall pressure distributions that are nearly identical to those predicted in the inviscid calculation. The overexpansion and recompression of the flow in the region $1<x/R<8$ have created negative as well as positive gradients caused by the discontinuity in the body curvature. Within this region, the present procedure of estimating average pressure gradient using $y^*=0.8$ is preferable to those straightforwardly lagging gradients. A comparison of the PNS and the BL heating rates is given in Fig. 5b. The metric factor needed in the BL calculation is found from the formula derived by DeJarnette.[20] Figure 5b shows that the two agree very well on the leeward pitch plane but very poorly on the windward plane, especially for $6<x/R<30$. The pressure gradient used in the PNS solution does not contribute much to the disagreement, as its value diminishes to zero beyond $x/R<12$. The dashed line in Fig. 5b shows the result of using $(p_x)_s$, where p_s is the shock pressure shown in Fig. 5a. The credibility of the present solution may be demonstrated partially by comparing the normalized heating rates $C_H/C_{H,x=0}$ with those measured by Cleary,[21] where $C_H=-q_y/\rho_\infty u_\infty(H_{T_\infty}-H_{T_w})$, the subscript T denoting the total condition. It shows that the normalized data are very close to the PNS results but lower than the BL results by as much as 50% at $x/R=10$. The skin friction coefficients $C_F=\pi_{yx}/\rho_\infty u_\infty^2$ and $\pi_{yz}/\rho_\infty u_\infty^2$ in the axial and circumferential directions are shown in Fig. 6. Good agreement is found in Fig. 6a between the PNS and the BL results. In Fig. 6b, the crossflow speed, as inferred from the skin friction coefficient, is seen to be decreasing as x increases. Likewise, the reverse flow inside the separate regions

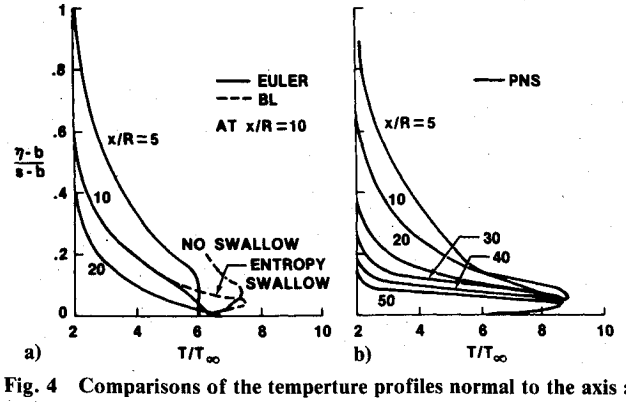

Fig. 4 Comparisons of the temperture profiles normal to the axis at various stations over a spherical cone at $M_\infty=8$, $Re_\infty=0.213\times10^6$/m, $R=0.105$ cm, and $T_w=5.6\ T_\infty$; a) inviscid and boundary-layer predictions, b) coupled inviscid-viscous predictions.

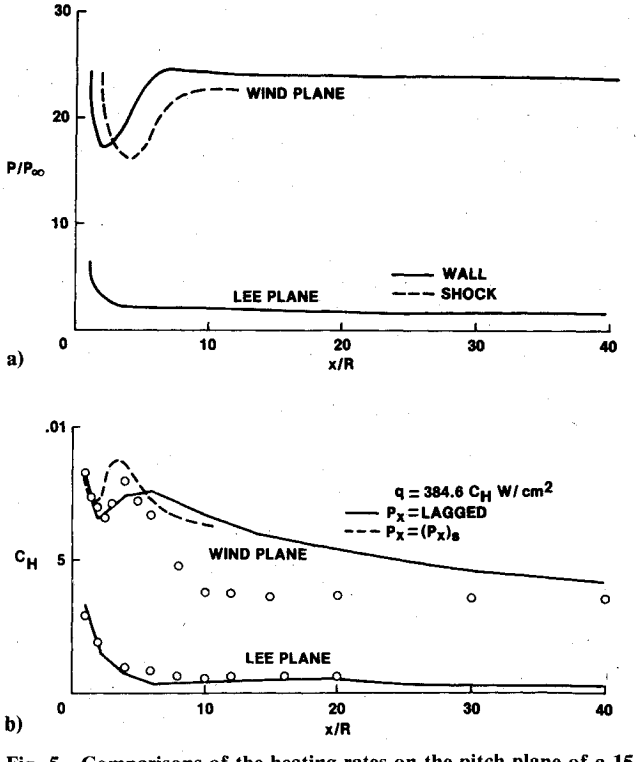

Fig. 5 Comparisons of the heating rates on the pitch plane of a 15-deg spherical cone at $M_\infty=8$, $\alpha=15$ deg, $Re_\infty=0.213\times10^6$/m, $R=0.105$ cm, and $T_w=5.6\ T_\infty$; a) wall pressure distributions, b) heating transfer coefficients obtained from the boundary-layer and the present theories.

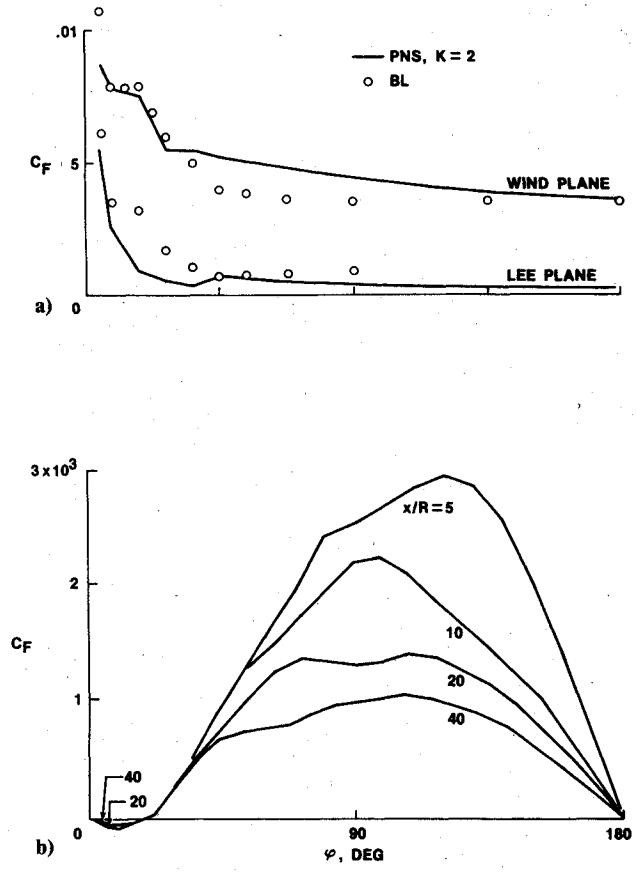

Fig. 6 Comparisons of wall friction coefficients between the boundary-layer and the present theories for a 15-deg spherical cone at $M_\infty = 8$, $\alpha = 15$ deg, $Re_\infty = 0.213 \times 10^6$/m, $R = 0.105$ cm, and $T_w = 5.6\ T_\infty$; a) streamwise distributions, b) circumferential distributions.

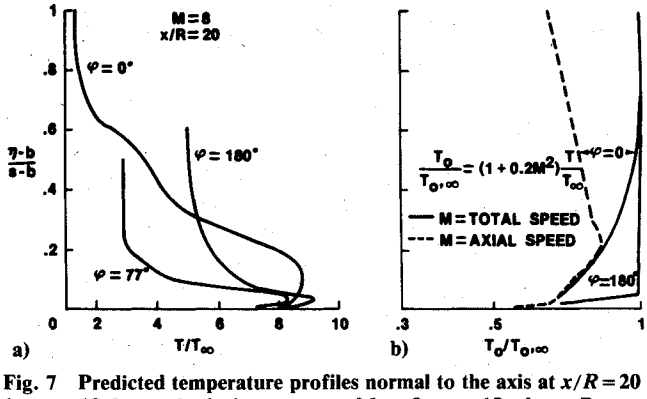

Fig. 7 Predicted temperature profiles normal to the axis at $x/R = 20$ for a 15-deg spherical cone at $M_\infty = 8$, $\alpha = 15$ deg, $Re_\infty = 0.213 \times 10^6$/m, $R = 0.105$ cm, and $T_w = 5.6\ T_\infty$; a) static temperature, b) total temperature.

has smaller speed for larger x. The total temperature profiles across the shock layer on the pitch plane, shown in Fig. 7b, can be used to delineate the boundary between the inviscid and viscous flows. The viscous layer as indicated is about 7% of the shock layer on the windward side and about 70% on the leeside. The total speed $(v^2 + w^2)^{1/2}$ must be used on the leeside to determine the total temperature because the radial component is almost as great as the axial component. The static temperature profiles shown in Fig. 7a differ drastically among the circumferential planes, although most of the windward planes have a temperature profile similar to that of an axisymmetric flow. The variation of temperature on the

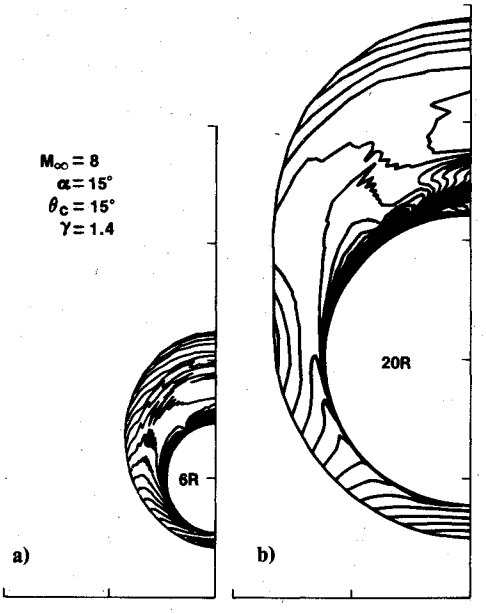

Fig. 8 An illustration of crossflow separation using the contours of crossflow speed at $x/R = 6$ and 20 for a 15-deg spherical cone at $M_\infty = 8$, $\alpha = 15$ deg, $Re_\infty = 0.213 \times 10^6$/m, $R = 0.105$ cm, and $T_w = 5.6\ T_\infty$.

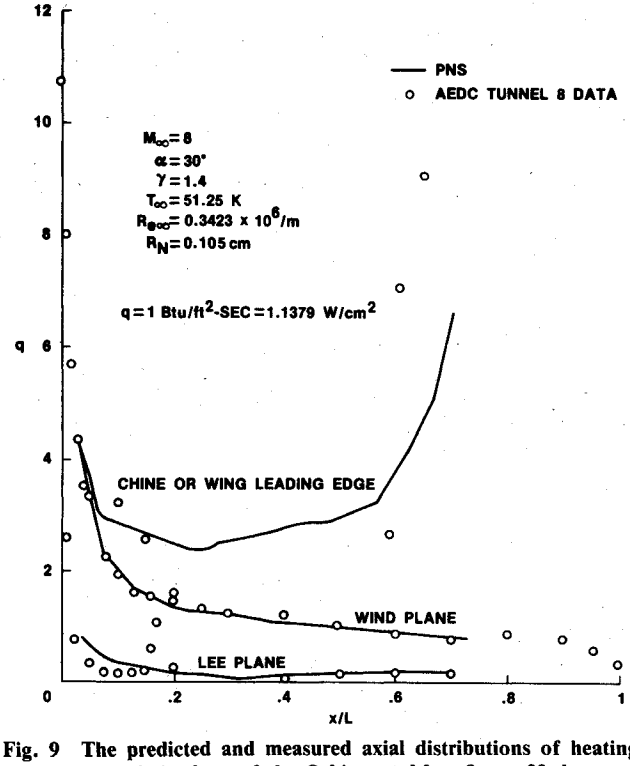

Fig. 9 The predicted and measured axial distributions of heating rates on the pitch plane of the Orbiter at $M_\infty = 8$, $\alpha = 30$ deg, and $Re_\infty = 0.335 \times 10^6$/m.

leeside pitch plane is of special interest. Not only does it show extensive interactions between the inviscid and the viscous flows but, for the relatively uniform pressure profile (not shown), it also displays the entropy variations. An attempt to exhibit the overall flowfield past a cone is made in Fig. 8, in which the contours of constant crossflow speed are shown at $x/R = 6$ and $x/R = 20$. The thick viscous layer on top of the cone is attached at $x/R = 6$ but is separated at $x/R = 20$. Note the faster growth of the viscous layer on the leeside than on the windward side of the cone.

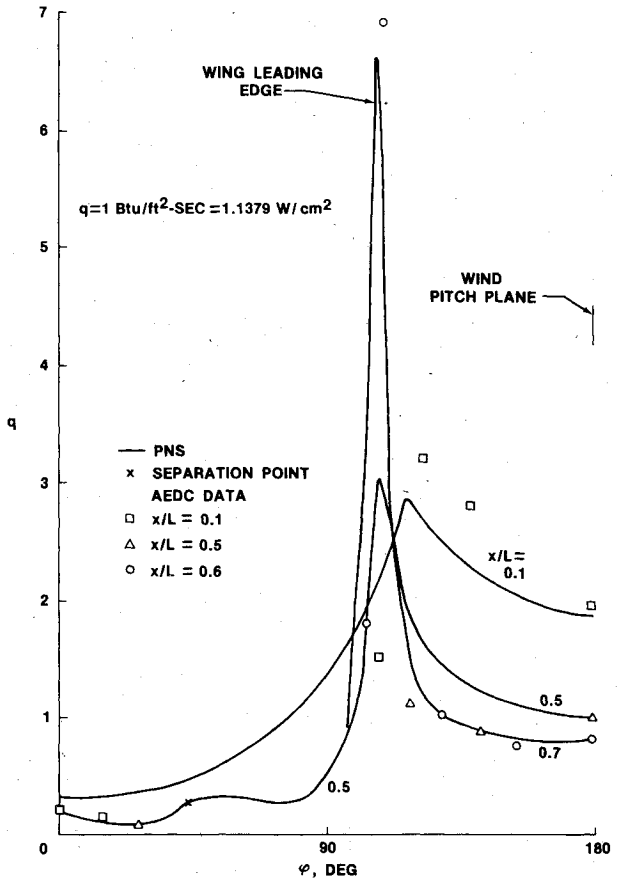

Fig. 10 The predicted and measured circumferential distributions of heating rates at three axial stations for the Orbiter at $M_\infty = 8$, $\alpha = 30$ deg, and $Re_\infty = 0.335 \times 10^6$/m.

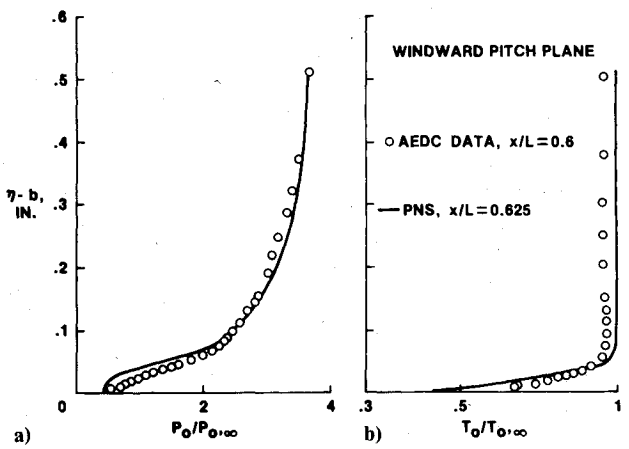

Fig. 11 Comparisons of the predicted and measured total pressure and total temperature profiles normal to the axis on the Orbiter at $x/L = 0.625$ at $M_\infty = 8$, $\alpha = 30$ deg, and $Re_\infty = 0.335 \times 10^6$/m; a) total pressure, b) total temperature.

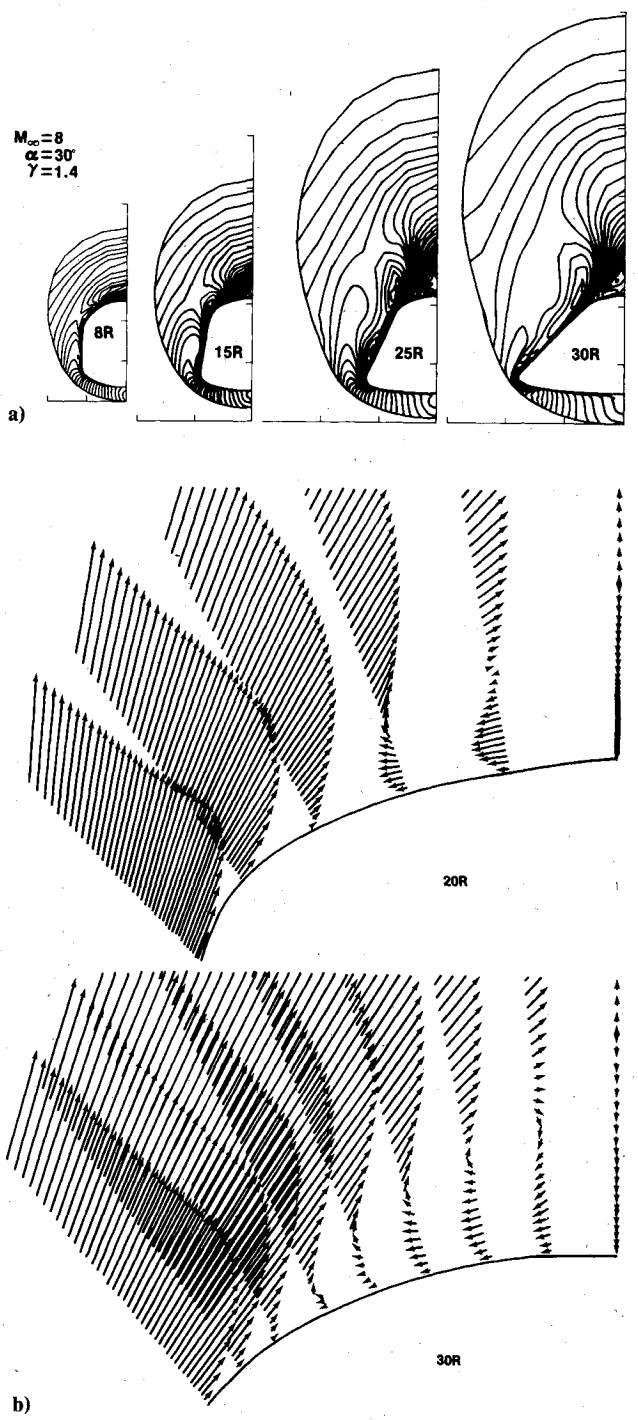

Fig. 12 An illustration of vortex growth on the leeside of the Orbiter at $M_\infty = 8$, $\alpha = 30$ deg, and $Re_\infty = 0.335 \times 10^6$/m; a) contours plots of crossflow speed at four stations, b) crossflow vectors at two stations.

Case 3 is concerned with the calculation of the flowfield around a delta-shaped Orbiter whose cross-sectional and longitudinal slopes are illustrated in Fig. 3b. The calculation is made for a 0.0175 scale model at $\alpha = 30$ deg with $\Delta x/R = 0.1$, $K = 2$, $c = 0.01$, and $y^* = 0.8$ from $x/R = 1$ to 33. Difficulties with convergence occur at the last station because of the bow-shock interaction with the wing leading edge. The computation takes 330 steps and about 3 h on a Univac 1110 computer, whereas the CPU/point equals 0.02 s. Several combinations of clustering parameters β and ω have been tested to see how the peak of heating and pressure near the chine and the wing can be resolved properly with a fixed number of grid points. Generally, a fine Δz is required for the calculation from the leeside pitch plane to a meridional plane underneath the bottom corner on the vehicle to provide adequate resolution for the separation flow on the top and the strong expansion around the corner. The first grid spacing adjacent to the wall needs readjustment at selective x stations to compensate for the increasing thickness of the shock layer. Consequently, the grid system is changed from 55×16 for $(y \times z)$ at $x/R = 1$ to 64×32 at $x/R = 33$.

The PNS results of the heating rate are in excellent agreement with the test data taken on the pitch planes.[18] The only difference is at $x/L = 0.15$ on the leeside where the

canopy is not included in the present body geometry. Figure 9 shows the heating rates as a function of x/L, L being the total length of the vehicle and equal to about 45 nose radii. The top line in Fig. 9 corresponds to the maximum value predicted by the PNS solution. The peak heating occurs at either the chine or the wing leading edge. Although there is an extensive body of experimental data, not many data points are yet available at those places because of the difficulty of installing instruments. The circumferential variations of heating are examined closely in Fig. 10. The highest heating at $x/L=0.7$ is caused by the shock-wing interaction, which also gives rise to the highest pressure at that station. The peak of heating at $x/L=0.5$ is caused by the rapid crossflow expansion over the chine, resulting in a sudden thinning of the boundary layer. The crossflow shock and the separating flow are responsible for the variations between $\phi=0$ and 70 deg at $x/L=0.5$, but the differences in the body contours in the model and the present geometry have caused the noticeable discrepancy on the windward side of the Orbiter. Figure 11 shows the detailed comparison of the viscous flow characteristics represented by pitot pressure and total temperature data across the layer at $x/L=0.6$ on the windward pitch plane. The agreement of the theory and the experiment[19] is very good considering the interference between the probe and the wall. The overall flowfield, featuring crossflow speed contours at several axial stations, is depicted in Fig. 12a. These plots display a much stronger vortex motion at $\alpha=30$ deg than the vortex formation at $\alpha=15$ deg for the cone. The crossflow vectors in Fig. 12b are useful to visualize the swirling motion and its growth along the x axis.

Concluding Remarks

An iterative factorization method for computing viscous shock-layer flows is developed and applied to re-entry bodies at high angles of attack. The accuracy of the results is found to depend on the initial data at the nose, the approximation made to the axial pressure gradient, the size of the step increment, and the grid system used on the axial plane. The Richtmyer scheme coupled with the iterative procedure yields stable and accurate results from the parabolic Navier-Stokes equations for a nonconical body with axial curvature. However, there is not much difference between the Laasonen and the Richtmyer schemes and between the iterative and the noniterative procedures in the results for conical bodies. The application to an Orbiter-like vehicle is very successful as the results agree favorably with the test data on the wall and, furthermore, describe a detailed flowfield unobtainable by previous boundary-layer approaches.

Appendix: Jacobian Matrices

$$A=\bar{A},\quad B=y_\xi\bar{A}+y_\eta\bar{B}+y_\zeta\bar{C},\quad C=\bar{C}$$

$$E=y_\xi^2\bar{D}+y_\eta^2\bar{E}+y_\zeta^2\bar{F},\ F=y_\zeta^2\bar{F}$$

$$A=\begin{bmatrix} u & \rho & 0 & 0 & 0 \\ u^2+ge & 2\rho u & 0 & 0 & g\rho \\ uv & \rho v & \rho u & 0 & 0 \\ uw & \rho w & 0 & \rho u & 0 \\ u(\epsilon+ge) & \rho(\epsilon+u^2+p/\rho) & \rho uv & \rho uw & (g+1)\rho u \end{bmatrix}$$

$g=0$ for $y>y^*$

$g=\gamma-1$ for $y\le y^*$

$$\bar{B}=\begin{bmatrix} v & 0 & \rho & 0 & 0 \\ vu & \rho v & \rho u & 0 & 0 \\ v^2+ge & 0 & 2\rho v & 0 & g\rho \\ vw & 0 & \rho w & \rho v & 0 \\ v(\epsilon+ge) & \rho uv & \rho(\epsilon+v^2+p/\rho) & \rho wv & (g+1)\rho v \end{bmatrix}$$

$$\bar{C}=\frac{1}{\eta}\begin{bmatrix} w & 0 & 0 & \rho & 0 \\ wu & \rho w & 0 & \rho u & 0 \\ wv & 0 & \rho w & \rho v & 0 \\ w^2+ge & 0 & 0 & 2\rho w & g\rho \\ w(\epsilon+ge) & \rho uw & \rho vw & \rho(\epsilon+w^2+p/\rho) & (g+1)\rho w \end{bmatrix}$$

$$\bar{D}=-\begin{bmatrix} 0 & 0 & 0 & 0 & 0 \\ 0 & 4\mu/3 & 0 & 0 & 0 \\ 0 & 0 & \mu & 0 & 0 \\ 0 & 0 & 0 & \mu & 0 \\ 0 & 4\mu u/3 & \mu v & \mu w & gk \end{bmatrix}$$

$$\bar{E}=-\begin{bmatrix} 0 & 0 & 0 & 0 & 0 \\ 0 & \mu & 0 & 0 & 0 \\ 0 & 0 & 4\mu/3 & 0 & 0 \\ 0 & 0 & 0 & \mu & 0 \\ 0 & \mu u & 4\mu v/3 & \mu w & gk \end{bmatrix}$$

$$\bar{F}=-\frac{1}{\eta^2}\begin{bmatrix} 0 & 0 & 0 & 0 & 0 \\ 0 & \mu & 0 & 0 & 0 \\ 0 & 0 & \mu & 0 & 0 \\ 0 & 0 & 0 & 4\mu/3 & 0 \\ 0 & \mu u & \mu v & 4\mu w/3 & gk \end{bmatrix}$$

Acknowledgments

The author is grateful for the support and interest given by W. D. Goodrich and R. Ried in the course of the study.

References

[1] Lubard, S. C. and Helliwell, W. S., "Calculation of the Flow on a Cone at High Angle of Attack," *AIAA Journal*, Vol. 12, July 1974, pp. 965-974.

[2] Lubard, S. C. and Rakich, J. V., "Calculations of the Flow on a Blunt Cone at High Angle of Attack," AIAA Paper 75-149, Jan. 1975.

[3] Helliwell, W. S., Dickinson, R. P., and Lubard, S. C., "Viscous Flow Over Arbitrary Geometries at High Angle of Attack," AIAA Paper 80-0064, Jan. 1980.

[4] Lin, T. C. and Rubin, S. G., "Viscous Flow Over a Cone at Moderate Incidence I. Hypersonic Tip Region," *Computer and Fluids*, Vol. I, Feb. 1973, pp. 37-57.

[5] Schiff, L. B. and Steger, J. L., "Numerical Simulation of Steady Supersonic Viscous Flow," AIAA Paper 79-0130, Jan. 1979.

[6] Vigneron, Y. C., Rakich, J. V., and Tannehill, J. C., "Calculations of Supersonic Flow Over Delta Wings with Sharp Subsonic Leading Edges," AIAA Paper 78-1138, Jan. 1978.

[7] Nardo, C. T. and Cresci, R. J., "An Alternating Directional Implicit Scheme for Three-Dimensional Hypersonic Flows," *Journal of Computational Physics*, Vol. 8, April 1971, pp. 268-284.

[8] Li, C. P., "A Computational Procedure for Supersonic Flows Governed by the Parabolic Navier-Stokes Equations," *Journal of Computational Physics*, Vol. 35, May 1980, pp. 356-380.

[9] Murray, A. L. and Lewis, C. H., "Viscous Shock-Layer Flows Over Bodies During Re-Entry," AIAA Paper 78-259, Jan. 1978.

[10] Beam, R. and Warming, R. F., "An Implicit Factored Scheme for the Compressible Navier-Stokes Equations," *AIAA Journal*, Vol. 16, April 1978, pp. 393-401.

[11] Chaussee, D. S., Patterson, J. L., Kutler, P., Pulliam, T. H., and Steger, J. L., "A Numerical Simulation of Hypersonic Viscous Flows Over Arbitrary Geometries at High Angle of Attack," AIAA Paper 81-0050, Jan. 1981.

[12] Kutler, P., Reinhardt, W. A., and Warming, R. F., "Multi-Shocked Three-Dimensional Supersonic Flowfields with Real Gas Effect," *AIAA Journal*, Vol. 11, May 1973, pp. 657-664.

[13] Richtmyer, R. D. and Morton, K. W., *Difference Methods for Initial-Value Problems*, 2nd ed., Interscience, New York, 1967.

[14] Pulliam, T. H. and Steger, J. L., "On Implicit Finite-Difference Simulattions of Three-Dimensional Flow," AIAA Paper 78-10, Jan. 1978.

[15] Briley, W. R. and McDonald, H., "Solution of the Multidimensional Compressible Navier-Stokes Equations by a Generalized Implicit Method," *Journal of Computational Physics*, Vol. 24, May 1977, pp. 372-397.

[16] Meyers, R. M., "User's Guide for a Three-Dimensional Aircraft Body Fit Program," Lockheed Electronics Co., Houston, Tex., TM-5060, 1975.

[17] Tong, H., Buckingham, A. C., and Curry, D. M., "Computational Procedure for Evaluation of Space Shuttle TPS Requirements," AIAA Paper 74-518, June 1974.

[18] Martindale, W. R., Kaul, C. E., and Nutt, K. W., "Test Results from the NASA/Rockwell International Space Shuttle Orbiter Heating Test (OH49B) Conducted in the AEDC-VKF Tunnel B," AEDC-DR-74-73, Sept. 1974.

[19] Carter, L. O. and Martindale, W. R., "Test Results from the NASA/Rockwell International Space Shuttle Test (OH9) Conducted in the AEDC-VKF Tunnel B," AEDC-DR-74-9, Jan. 1974.

[20] DeJarnette, F. R. and Davis, R. M., "A Simplified Method for Calculating Laminar Heat Transfer Over Bodies at an Angle of Attack," NASA TN D-4720, 1968.

[21] Cleary, J. W., "Effects of Angle of Attack and Bluntness on Laminar Heating-Rate Distributions of a 15° Cone at a Mach Number of 10.6," NASA TN D-5450, 1969.

From the AIAA Progress in Astronautics and Aeronautics Series

RAREFIED GAS DYNAMICS—v. 74 (Parts I and II)

Edited by Sam S. Fisher, University of Virginia

The field of rarefied gas dynamics encompasses a diverse variety of research that is unified through the fact that all such research relates to molecular-kinetic processes which occur in gases. Activities within this field include studies of (a) molecule-surface interactions, (b) molecule-molecule interactions (including relaxation processes, phase-change kinetics, etc.), (c) kinetic-theory modeling, (d) Monte-Carlo simulations of molecular flows, (e) the molecular kinetics of species, isotope, and particle separating gas flows, (f) energy-relaxation, phase-change, and ionization processes in gases, (g) molecular beam techniques, and (h) low-density aerodynamics, to name the major ones.

This field, having always been strongly international in its makeup, had its beginnings in the early development of the kinetic theory of gases, the production of high vacuums, the generation of molecular beams, and studies of gas-surface interactions. A principal factor eventually solidifying the field was the need, beginning approximately twenty years ago, to develop a basis for predicting the aerodynamics of space vehicles passing through the upper reaches of planetary atmospheres. That factor has continued to be important, although to a decreasing extent; its importance may well increase again, now that the USA Space Shuttle vehicle is approaching operating status.

A second significant force behind work in this field is the strong commitment on the part of several nations to develop better means for enriching uranium for use as a fuel in power reactors. A third factor, and one which surely will be of long term importance, is that fundamental developments within this field have resulted in several significant spinoffs. A major example in this respect is the development of the nozzle-type molecular beam, where such beams represent a powerful means for probing the fundamentals of physical and chemical interactions between molecules.

Within these volumes is offered an important sampling of rarefied gas dynamics research currently under way. The papers included have been selected on the basis of peer and editor review, and considerable effort has been expended to assure clarity and correctness.

1248 pp., 6×9, illus., $55.00 Mem., $95.00 List

TO ORDER WRITE: Publications Dept., AIAA, 1290 Avenue of the Americas, New York, N.Y. 10104